
Two-Photon Conversion of a Bacterial Phytochrome

S. G. Sokolovski, E. A. Zherebtsov, R. K. Kar, D. Golonka, R. Stabel, N. B. Chichkov, A. Gorodetsky, I. Schapiro, A. Möglich*, E. U. Rafailov*

* corresponding authors:

E.U.R. e.rafailov@aston.ac.uk; A.M. andreas.moeglich@uni-bayreuth.de

Abstract

In nature, sensory photoreceptors underlie diverse spatiotemporally precise and generally reversible biological responses to light. Photoreceptors also serve as genetically encoded agents in optogenetics to control by light organismal state and behavior. Phytochromes represent a superfamily of photoreceptors that transition between states absorbing red light (Pr) and far-red light (Pfr), thus expanding the spectral range of optogenetics to the near-infrared range. Although light of these colors exhibits superior penetration of soft tissue, the transmission through bone and skull is poor. To overcome this fundamental challenge, we explore the activation of a bacterial phytochrome by a femtosecond laser emitting in the 1 μm wavelength range. Quantum chemical calculations predict that bacterial phytochromes possess substantial two-photon absorption cross sections. In line with this notion, we demonstrate that the photoreversible $\text{Pr} \leftrightarrow \text{Pfr}$ conversion is driven by two-photon absorption at wavelengths between 1170 and 1450 nm. The Pfr yield was highest for wavelengths between 1170 and 1280 nm and rapidly plummeted beyond 1300 nm. By combining two-photon activation with bacterial phytochromes, we lay the foundation for enhanced spatial resolution in optogenetics and unprecedented penetration through bone, skull and soft tissue.

Keywords

Bacterial phytochrome; Nonlinear activation; Optogenetics; Photoconversion; Sensory photoreceptor; Two-photon absorption; Ultra-short pulses

28 Statement of Significance

29 Sensory photoreceptor proteins mediate vital physiological adaptations to light. In optogenetics, they serve
30 as light-gated actuators to enable the control of cellular state and physiology with precision in time and
31 space. The application of optogenetics to entire organisms, especially within the brain, remains challenging,
32 to a large extent owing to poor penetration of visible light through tissue and bone. To address this
33 fundamental challenge, we here investigate the actuation of a bacterial phytochrome photoreceptor via
34 two-photon (2P) absorption of femtosecond laser radiation of micrometer wavelengths. 2P absorption
35 drives the bidirectional photoconversion between two activity states of the phytochrome. By principally
36 demonstrating the validity of 2P actuation, our study paves the way towards optogenetic applications with
37 enhanced penetration depth and spatial resolution.

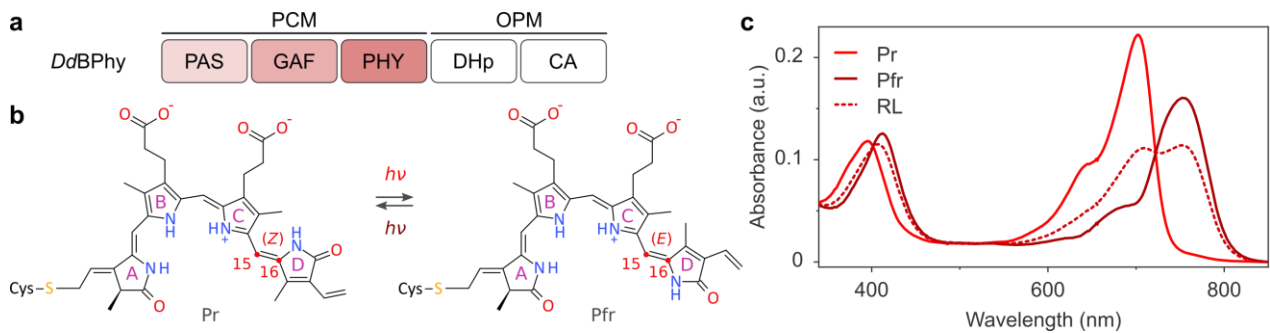
38

39 Introduction

40 Light-dependent adaptations of physiology, behavior and development in nature are mediated by sensory
41 photoreceptor proteins (1, 2). Sensitivity to specific bands of the electromagnetic spectrum is provided by
42 chromophores, small aromatic compounds embedded within the photoreceptor. The light-dependent
43 responses elicited by sensory photoreceptors generally exhibit characteristic hallmarks: they are precise in
44 time and space; they are reversible; and they are fully genetically encoded. For precisely these traits,
45 sensory photoreceptors double as actuators for the manipulation by light of cellular state and physiology in
46 optogenetics (3). Originating in the neurosciences, optogenetics has become a powerful approach across
47 many areas of biology, allowing to tackle unresolved questions in unprecedented ways. Although initially
48 optogenetics was confined to a small set of naturally occurring opsin photoreceptors, foremost the ion-
49 conducting channelrhodopsins (4, 5), since the repertoire of available actuators has been greatly expanded
50 by other photoreceptor classes and by protein engineering. In this manner, a multitude of cellular
51 processes has been unlocked for optogenetic intervention beyond the opsin-based control of the ion
52 distribution across the plasma membrane (6). Despite these advances, the application of optogenetics in
53 the brain of living animals remains demanding. To surmount these challenges, there has been a push
54 towards actuators that can be activated more effectively, because either they respond to longer
55 wavelengths with better tissue penetration (7, 8), they exhibit extended lifetimes of their active states (9),
56 or both. Phytochrome photoreceptors (Phys) in principle provide a viable alternative as they intrinsically
57 respond to longer wavelengths than opsins do and thereby expand the spectrum available for optogenetic
58 actuation into the red and near-infrared region (10). Light within this region falls in the near-infrared
59 spectral window and displays enhanced penetration of soft tissue (11), thereby rendering phytochromes
60 attractive for optogenetics.

61 First discovered in land plants (12), phytochromes are a class of sensory photoreceptors that underpin
62 manifold adaptive responses to red and near-infrared light across plants, algae, bacteria and fungi (13, 14).
63 At the molecular level, Phys generally exhibit bipartite architecture with an N-terminal photosensory core
64 module (PCM) that processes light signals, and a C-terminal output module that exerts downstream
65 physiological responses (Fig. 1a).

66



67

68 **Figure 1** | Architecture and photochemistry of the *Deinococcus deserti* bacteriophytochrome (*DdBPhy*). **a**,
 69 *DdBPhy* consists of a photosensory core module (PCM) with consecutive PAS, GAF and PHY domains, and of
 70 an output module (OPM) that comprises DHp and CA domains and acts as a histidine kinase. **b**, In darkness,
 71 the *DdBPhy* PCM predominantly adopts the red-absorbing Pr state with the biliverdin chromophore in its
 72 15Z conformation. Red light drives isomerization to the 15E conformation, leading to the population of the
 73 far-red-absorbing Pfr state. Far-red (or, near-infrared) light drives the reverse Pfr→Pr reaction. **c**, Pr and Pfr
 74 absorbance spectra of the *DdBPhy* PCM. The dashed line (RL) denotes the mixed-state spectrum obtained
 75 at photostationary state under illumination with red light [(680 ± 15) nm].

76 The Phy PCM generally consists of serial PAS (Per-ARNT-Sim, (15)), GAF (cGMP-specific phosphodiesterase,
 77 adenylyl cyclase and FhIA, (16)) and PHY (PHY-specific, (17, 18)) domains. To enable absorption of light in
 78 the red to near-infrared spectral range, Phys covalently bind within their GAF domains linear tetrapyrrole
 79 (i.e. bilin) chromophores (Fig. 1b). Phys cycle between two states denoted Pr and Pfr that absorb red and
 80 far-red light, respectively, and that differ in the configuration of their chromophore. Within the Pr state, the
 81 bilin chromophore assumes the Z isomer of its C15=C16 double bond. Absorption of red light drives the
 82 Pr→Pfr transition that is characterized by bilin isomerization to the 15E state, and far-red light promotes
 83 the reverse Pfr→Pr reaction. In conventional Phys, the Pr state is thermodynamically more stable than Pfr
 84 and prevails in darkness. By contrast, the so-called bathyphytochromes assume the Pfr form as their dark-
 85 adapted state. The 15Z/E isomerization underlying the Pr→Pfr transition triggers the refolding of a
 86 protrusion of the PHY domain, termed PHY tongue, from a β-hairpin to an α-helical conformation, and
 87 thereby induces quaternary structural rearrangements within the homodimeric Phy PCM (19–21). The
 88 nature and mode of action of the output module differ between bacterial and plant Phys. In bacterial Phys
 89 (BPhys), the output module comprises effector units that directly mediate the biological output, often
 90 enzymatic in nature. By contrast, plant Phys generally elicit physiological responses through light-
 91 dependent nuclear translocation, protein degradation and protein:protein interactions with intracellular
 92 partners, particularly the phytochrome-interacting factors (22–25). Bacterial and plant Phys further differ in
 93 the type and attachment site of their bilin chromophores. Whereas BPhys covalently attach biliverdin (BV)
 94 to a cysteine at the PAS N-terminus, plant Phys incorporate a derivative of BV, phytochromobilin, bound to
 95 a cysteine within the GAF domain (13). Due to the more extended conjugated π electron system of BV,
 96 BPhys exhibit a bathochromic shift of their Pr and Pfr states relative to those of plant Phys. Moreover, BV
 97 widely occurs in mammalian tissue (26–30), unlike phytochromobilin or the cyanobacterial phycocyanobilin
 98 that plant Phys can also accommodate.

99 Both bacterial and plant Phys have witnessed use in optogenetics (31). Of particular advantage, the
 100 bimodal toggling of Phys between (meta)stable states of different activity by two light colors can be
 101 leveraged for enhanced optogenetic resolution in time and space (32). As Phys respond to comparatively
 102 long wavelengths, they can be actuated within the near-infrared spectral window where light exhibits
 103 superior soft tissue penetration (11). Owing to the availability of BV in mammals (26, 29, 33), BPhys are

104 principally suitable for *in vivo*-optogenetics in living animals. To this end, several BPhy-based optogenetic
105 actuators have been built by protein engineering (10, 31). On the one hand, a collection of BPhy receptors
106 (27, 29, 30, 34) act as photoactivated nucleotidyl cyclases and catalyze the formation of cyclic mono- and
107 dinucleotides that serve as second messengers in eukaryotes and prokaryotes. In a similar vein, we
108 constructed light-activated BPhy-phosphodiesterases that hydrolyze cyclic mononucleotides (26, 35). On
109 the other hand, certain BPhy receptors enter light-dependent protein:protein interactions which have been
110 harnessed to optogenetically control subcellular localization and gene expression (36, 37).

111 Although phytochromes respond to comparatively long wavelengths and exhibit bimodal $Pr \leftrightarrow Pfr$
112 switching, their optogenetic deployment in the brain remains challenging, particularly owing to limited skull
113 and bone penetration of visible to near-infrared light. To overcome this restriction and to thus enable
114 transcranial actuation of phytochrome photoreceptors, we envision nonlinear activation of phytochromes
115 by a femtosecond pulsed laser with near-infrared wavelengths of 1000-1450 nm (38). Notably, light of
116 these wavelengths offers better penetration through the skull (39, 40), thus significantly increasing the
117 accessible depth in brain tissue. Two-photon (2P) excitation was previously applied to a set of modified
118 bacterial phytochrome variants to evoke fluorescence (41), thus demonstrating that phytochromes can be
119 optically excited in a nonlinear regime. However, these studies focused on incapacitated receptors
120 optimized for enhanced fluorescence quantum yield but impaired in their photochemistry. As a corollary,
121 the experiments did not uncover whether $Pr \rightarrow Pfr$ photoconversion, as opposed to fluorescence, can be
122 driven by 2P irradiation, and if so, to what extent. To assess these fundamental aspects and thereby gauge
123 the principal feasibility of nonlinearly activating phytochrome receptors, we here investigated the actuation
124 of a bacterial Phy in the two-photon regime (42–45).

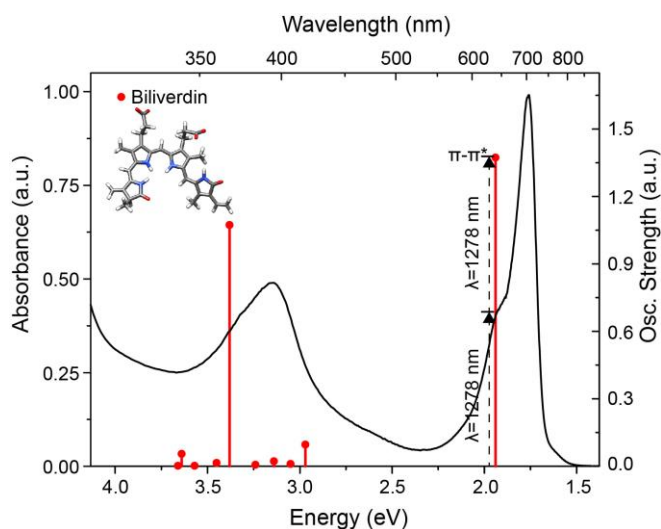
125

126 Results

127 Among the first-described bacterial phytochromes (46–48), the BPhy from *Deinococcus radiodurans* has
128 been widely studied in terms of function, photochemistry, mechanism and structure (19, 20, 49–51). As a
129 consequence, a set of engineered photoreceptors are based on the *D. radiodurans* PCM (*DrPCM*), especially
130 for the regulation of cyclic mononucleotides (26, 29, 30). However, several of these receptors suffered from
131 impaired light-dependent regulation, in that far-red light could not fully counteract prior activation by red
132 light. In the context of a photoactivated adenylyl cyclase (27), we recently found that fully photoreversible,
133 bidirectional switching of enzymatic activity could be attained via exchange of the *DrPCM* for the
134 homologous PCM of *Deinococcus deserti* BPhy (*DdPCM*). Although the underlying molecular reasons remain
135 elusive, *DdPCM* evidently improved the performance, and therefore we focused on this variant. To this end,
136 we heterologously expressed the *DdPCM* in *Escherichia coli* and analyzed it by UV/vis spectroscopy (Fig. 1c).
137 In its dark-adapted state, *DdPCM* predominantly adopted its Pr form, characterized by Soret and Q
138 absorption bands at around 390 and 700 nm, respectively. Irradiation with red light [(680 ± 15) nm]
139 partially populated the Pfr state with a Q-band absorption around 750 nm. Notably, under saturating 680-
140 nm light, a steady-state Pfr:Pr mixture of 0.69:0.31 was achieved (Fig. 1c, dashed line). Put another way,
141 light drives both the $Pr \rightarrow Pfr$ and the $Pfr \rightarrow Pr$ transitions, and a photostationary state is reached. Subsequent
142 exposure to far-red light [(780 ± 15) nm] restored the original dark-adapted spectrum. We next monitored
143 the thermal recovery to the dark-adapted Pr state after prior exposure to red light. At 22°C, the slow
144 recovery kinetics could be fitted by a sum of two exponential functions with rate constants of $k_1 = (1.60 \pm$
145 $0.01) \times 10^{-2} \text{ min}^{-1}$ and $k_2 = (2.01 \pm 0.01) \times 10^{-4} \text{ min}^{-1}$ (Supporting Information Fig. S1).

146 Quantum Chemical Calculation of Two-photon Absorption

147 We next calculated electronic excitation spectra for the *DdPCM* to assess nonlinear actuation by two-
148 photon irradiation. As no high-resolution structure is available yet for *DdPCM*, we generated a homology
149 model for the dark-adapted Pr state based on the structure of the *DrPCM* (52) (Supporting Information Fig.
150 S2). Using the hybrid quantum mechanics/molecular mechanics (QM/MM) method, we first calculated one-
151 photon absorption (1PA) spectra of the Pr form of *DdPCM* (Fig. 2).



152

153 **Figure 2** | The experimentally measured Pr absorbance spectrum of *DdPCM* (black line) and the calculated
154 vertical excitation energies in stick representation. The height of the sticks is determined by the oscillator
155 strength. The two-photon excitation energy is marked as a dashed stick. The optimized geometry of the
156 biliverdin chromophore is shown in the inset.

157 In the simulations, the QM region either encompassed all atoms of the biliverdin chromophore or excluded
158 the propionate sidechains (QM65). This choice is justified by the analysis of the molecular orbitals involved
159 in the electronic transitions (Supporting Information Fig. S3), which are localized exclusively on the four
160 pyrrole rings. Hence, the electronic transitions do not involve the propionate side chains as they are not a
161 part of the conjugated π electron system. This signifies that the size of QM region, or more specifically the
162 inclusion of the propionate chains, has no impact on the absorbance peaks.

163 The excitation energy for the $S_0 \rightarrow S_1$ transition, corresponding to the Q band, is found at 1.94 eV (642 nm).
164 This value overestimates the experimental one of 1.77 eV (700 nm) by 0.17 eV, well within the error range
165 of the method (53). The excitation energy for the transition that gives rise to the Soret band is found at
166 3.38 eV (368 nm), consistently overestimating the experimental peak at 3.18 eV (390 nm) by 0.2 eV. In
167 these simulations, the Q band constitutes transition to the S_1 state while the Soret band corresponds to
168 that to the S_6 state. There are, however, additional excited states between the Q and Soret bands that have
169 very small oscillator strength and are hence called dark states (Fig. 2). The shoulder of the Soret band is due
170 to the vibronic coupling, as evidenced by experiments and simulation (54). This is also confirmed by our
171 simulation, since no additional excited state close to S_1 was found. The full description of the excited states,
172 the oscillator strengths and the frontier orbitals are provided in the Supporting Information Table S1. The
173 oscillator strength of the transitions correlates with the relative intensities of the corresponding Soret and
174 Q bands in the experimental spectrum (Table 1).

175 **Table 1** | Calculated 1PA and 2PA excitation energies for the Q and Soret bands. The calculations were
176 performed at the RI-CC2/aug-cc-pVDZ level of theory.

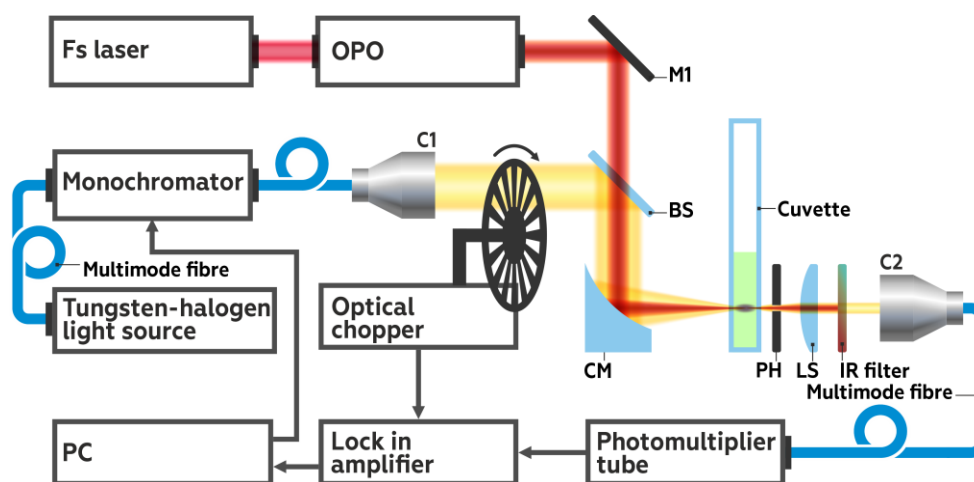
Biliverdin	1PA		2PA		
	Energy (eV)	Oscillator Strength (<i>f</i>)	Energy (eV)	δ^{TPA} (a.u.)	σ^{TPA} (GM)
Q band	1.94	1.374	0.97	6757	9.309
Soret band	3.38	1.074			

177

178 We then calculated the 2PA energy for the first bright state as summarized in Table 1. To this end, we used
 179 the RI-CC2 method which has been assessed for the calculation of two-photon absorption (2PA) of protein-
 180 embedded chromophores (55, 56). The calculated 2PA energies are degenerate in nature and correspond
 181 to half of the excitation energy obtained from 1PA calculations. δ^{TPA} corresponds to the two-photon
 182 transition moment and is directly proportional to the 2PA cross section (σ^{TPA}) in GM (Goepfert Mayer)
 183 units. δ^{TPA} was 6757 a.u. and the calculated σ^{TPA} obtained from the simulation was 9.309 GM. Taken
 184 together, the QM/MM calculations predict that the *DdPCM* can be actuated by 2PA with energies around
 185 0.97 eV, corresponding to a wavelength of 1278 nm. Notably, the truncation of the propionate side chains
 186 has no significant effect on the calculated vertical excitation energies (Supporting Information Fig. S4, Table
 187 S2 and supporting results).

188 Two-photon Conversion of *DdPCM*

189 We experimentally tested and characterized the effect of nonlinear activation of *DdPCM* by a femtosecond
 190 pulsed laser emitting between 1170 and 1450 nm. To this end, we developed an optical setup (Fig. 3) that
 191 integrates linear, one-photon and nonlinear, two-photon (2P) irradiation, and allows the confocal
 192 measurement of absorbance changes.



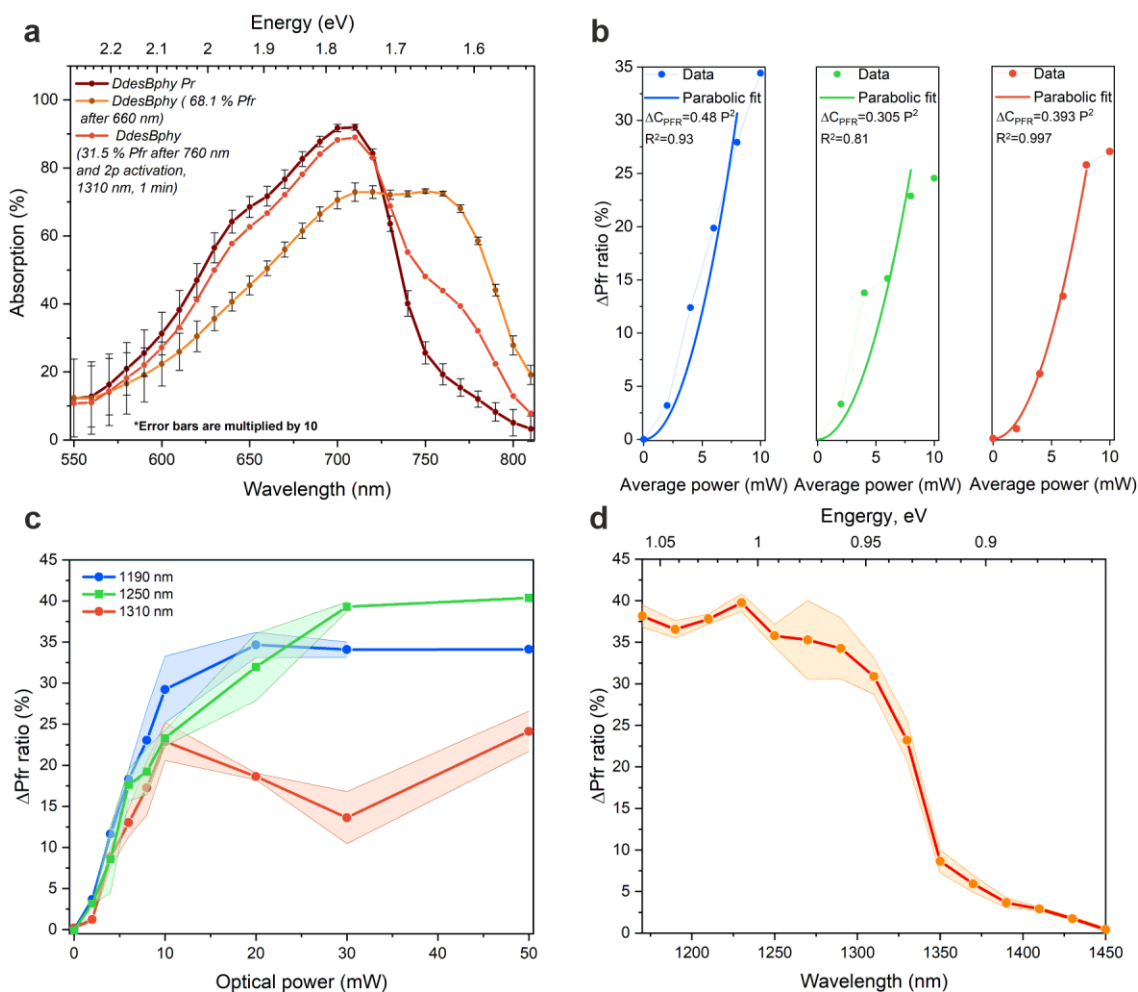
193

194 **Figure 3** | Schematic representation of the instrumental setup consisting of a subsystem for two-photon
 195 phytochrome activation at 1170 – 1450 nm spectral range and a channel for confocal absorbance
 196 measurements in the spectral range of 550 – 810 nm. Abbreviations are OPO, optical parametric oscillator;
 197 M1, mirror; BS, dichroic mirror; CM, concave mirror; PH, pinhole; LS, collecting lens; C1 and C2, collimators.

198 We used an optical parametric amplifier (TOPAS Prime, Coherent) pumped with a Ti:sapphire laser
 199 (Astrella, Coherent) to deliver pulses of ~50 fs width at a repetition rate of 4 kHz, tunable wavelengths
 200 between 1170 – 1450 nm and average optical powers up to ~50 mW (peak power ~235 MW). After passing
 201 through a dichroic mirror, the fs laser pulses are reflected from a concave mirror ($f = 200$ mm, radius of
 202 curvature 400 mm) and thereby focused on a spot inside a sample cuvette of 1 mm thickness. To measure
 203 absorbance changes associated with the phytochrome Pr→Pfr transformation within the focal area, we

204 implemented synchronous, confocal detection by ultra-low-power probe radiation in the spectral range of
 205 550 – 810 nm. To this end, the probe beam was collimated and co-aligned with the micrometer laser
 206 radiation via the dichroic mirror and two pinholes placed after and at the center position of the cuvette.
 207 After the alignment, the latter pinhole was removed, and the cuvette holder was installed. The collecting
 208 lens and the collimator gathered the transmitted probe light, while an IR filter prevented the laser beam
 209 from hitting the photomultiplier detector.

210 For the measurements, we used a *DdPCM* concentration of 50 μM . The temperature inside the cuvette was
 211 monitored by a miniature thermocouple placed near the focal spot. Notably, measurements by the
 212 thermocouple might hence somewhat underestimate the actual temperature increase within the focal
 213 spot. In a control experiment using the highest laser power of 50 mW, the temperature increase was less
 214 than 2°C. To initially toggle the phytochrome between its Pr and Pfr forms, we exposed the cuvette to LEDs
 215 emitting at 766 and 680 nm, respectively (Fig. 4a). Using these LEDs to drive the linear $\text{Pr} \leftrightarrow \text{Pfr}$
 216 photoconversion, the sample integrity could be assessed between measurements and *DdPCM* could be
 217 transformed to its Pr state for subsequent nonlinear photoconversion. To this end, we subjected the
 218 sample in its Pr state to the fs laser pulses and recorded the resultant absorbance changes immediately
 219 afterwards. In line with an earlier report (41), the laser radiation elicited fluorescence of the sample. Upon
 220 irradiation with laser pulses in the spectral range of 1170-1450 nm for 1 minute, the *DdPCM* samples
 221 exhibited characteristic absorbance changes (Fig. 4a), with the peak at around 700 nm decreasing and a
 222 new one forming at around 750 nm. Based on comparison to the absorbance spectra of *DdPCM* in its Pr and
 223 Pfr states (see Fig. 1c), we assign these changes as $\text{Pr} \rightarrow \text{Pfr}$ conversion of the phytochrome molecules by
 224 multiphoton absorption.



225

226 **Figure 4** | Nonlinear Pr→Pfr photoconversion of *DdPCM*. **a**, Absorbance spectra of *DdPCM* upon irradiation
227 with 660-nm (yellow line) and 766-nm (dark red line) light. The red line denotes the absorbance spectrum
228 obtained after two-photon photoconversion using fs laser irradiation at 1310 nm; **b**, Amount of Pfr state
229 generated by 2P photoconversion in the regime of lower optical powers at wavelengths of 1190 nm (blue),
230 1250 nm (green) and 1310 nm (red). The lines represent fits to parabolic functions; **c**, Power dependence of
231 the two-photon photoconversion over a broader pump power range; **d**, Dependence of the maximal
232 absorbance changes of *DdPCM* on 2P irradiation wavelength.

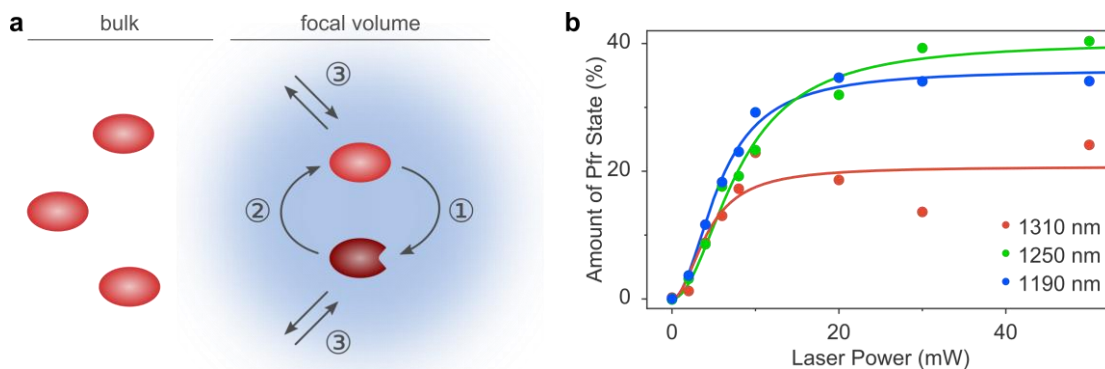
233 To verify that it is two-photon absorption that drives the Pr→Pfr conversion of *DdPCM*, we applied various
234 power intensities. In the intensity regime below 10 mW, the yield of Pfr state increased with power
235 approximately quadratically (Fig. 4b), which indicates that the Pr→Pfr transition is induced by two-photon
236 absorption. At higher powers above 10 mW, the Pfr yield approached a plateau (Fig. 4c). Neither extending
237 the time of irradiation nor increasing the power beyond approximately 10-20 mW enhanced the Pfr yield
238 further. We next analyzed the wavelength dependence of the Pr→Pfr conversion in the two-photon
239 regime. To this end, we assessed to which extent illumination from 1170 nm to 1450 nm is capable of
240 effectively transforming *DdPCM* from its Pr to the Pfr state (Fig. 4d). The Pr→Pfr conversion remained
241 relatively constant at around 35% over the range of 1170-1300 nm but plummeted to about 20% or lower
242 for wavelengths above 1300 nm.

243

244 Discussion

245 Our hybrid quantum mechanical/molecular mechanics simulations clearly suggest that *DdPCM* and, by
246 extension, likely other bacterial phytochromes possess appreciable two-photon absorption cross sections in
247 the micrometer wavelength range. In line with this notion, an earlier study demonstrated two-photon
248 fluorescence for a set of bacterial phytochromes and thereby provided important benchmarks for their use
249 as novel, genetically encodable fluorophores emitting in the red to near-infrared spectral range (41).
250 However, the phytochromes under study were deliberately incapacitated in their Pr→Pfr photoconversion,
251 such as to enhance fluorescence quantum yield. It thus remained unclear whether two-photon absorption
252 can efficiently drive the Pr→Pfr photoconversion. To fill this principal gap in our knowledge, we devised an
253 optical setup that integrates pulsed, femtosecond two-photon excitation with confocal absorbance readout
254 to assess the degree of photoconversion. Our data reveal that two-photon irradiation can not only elicit
255 fluorescence in phytochromes, as reported earlier, but also drives their productive Pr→Pfr
256 photoconversion.

257 To arrive at a better understanding of the underlying processes and their implications, we sought to
258 globally analyze the experimental data by a phenomenological mechanistic model of two-photon
259 photoconversion (Fig. 5a).



260

261 **Figure 5** | Quantitative analysis of two-photon photoconversion in *DdPCM*. **a**, Reaction sequence under
 262 two-photon irradiation. Inside the focal volume, the *DdPCM* is converted from its initial Pr state (red
 263 ellipsoids) to its Pfr state (dark red) via two-photon photoconversion (process ①). The 2P irradiation
 264 simultaneously drives the Pfr→Pr reverse process (②). During the experiment, *DdPCM* diffuses out of the
 265 focal volume into the surrounding, much larger bulk volume and *vice versa* (③). At the start of the
 266 experiment, the *DdPCM* resides completely in its Pr state. **b**, The circles denote the experimental data from
 267 Fig. 4c, and the solid lines represent a global fit to the model shown in panel a.

268 The model considers three elementary reactions: 1. Pr→Pfr photoconversion within the focal volume; 2. a
 269 process returning the Pfr state to Pr within the focal volume; and 3. diffusion between the focal volume and
 270 the considerably larger bulk volume. We modelled the forward Pr→Pfr reaction as a two-photon process,
 271 based on principal considerations and supported by the approximately quadratic power dependence of
 272 photoconversion yields at lower intensities (Fig. 4b). Whereas this process (reaction 1) evidently increases
 273 the Pfr amount inside the focal volume, diffusional exchange (reaction 3) with the surrounding bulk
 274 volume, which contains *DdPCM* fully in its Pr state, leads to a net decrease. The competition between
 275 reactions 1 and 3 (see Fig. 5a) during 2P irradiation explains why at a given wavelength and power, the Pfr
 276 yield does not increase beyond a certain illumination time. Strikingly, our data revealed that the Pfr yield
 277 asymptotically approaches plateau values between 20 and 40%, depending on wavelength. This
 278 observation directly implies that there is a return process (reaction 2) that depletes the Pfr state.
 279 Moreover, the fact that a constant plateau is reached indicates that this return reaction has the same
 280 power dependence on 2P irradiation intensity as the forward reaction 1. In analogy to the linear excitation
 281 regime where red-light exposure results in a photostationary Pr:Pfr mixture (see Fig. 1c), we deem two-
 282 photon Pfr→Pr photoconversion the most likely candidate for the return process 2.

283 To ascertain whether the experimental data conform to this mechanistic model, we globally analyzed them
 284 according to the reaction scheme in Fig. 5a (see Methods). The Pfr yield reached inside the focal volume at
 285 photostationary state, FR_{∞} , is given by equations (1) and (2).

$$286 \quad FR_{\infty} = R_0 + FR_0 - k_{-1}/\tilde{k} \times (R_0 + FR_0) + D/\tilde{k} \times R_0 \quad (1)$$

$$287 \quad \tilde{k} = k_1 + D + k_{-1} \quad (2)$$

288 where $R_0 = 1$ and $FR_0 = 0$ are the Pr and Pfr fractions in the absence of irradiation, and k_1 , k_{-1} and D denote
 289 the rate constants for the Pr→Pfr photoconversion, the Pfr→Pr reversion, and the diffusional exchange,
 290 respectively. The rate constants for the forward and reverse photoconversion k_1 and k_{-1} are taken to scale
 291 with the square of the photon flux Φ inside the focal volume which in turn is related to the applied laser
 292 power P according to equation (3).

$$\Phi = g_{\lambda} \times P \quad (3)$$

294 where the constant g_{λ} accounts for the difference in relative photon energy and flux density within the
295 focal volume for the individual wavelengths.

296 As is apparent from equation (1), the Pfr yield reached at photostationary equilibrium for a given
297 wavelength and power does not depend on the absolute velocities k_1 , k_{-1} and D of the individual reactions
298 but rather on their ratios. We hence fixed the diffusion rate constant at an arbitrary value of $D = 1$. A global
299 fit of the power dependency data at wavelengths of 1190, 1250 and 1310 nm then yielded parameter
300 values of $k_1^{1190} = (1.1 \pm 0.2) \times 10^{-2} \text{ mW}^{-2} \times P^2$, $k_{-1}^{1190} = (2.0 \pm 0.4) \times 10^{-2} \text{ mW}^{-2} \times P^2$, $k_1^{1250} = (6.4 \pm 0.9) \times 10^{-3}$
301 $\text{mW}^{-2} \times P^2$, $k_{-1}^{1250} = (9.5 \pm 1.8) \times 10^{-3} \text{ mW}^{-2} \times P^2$, $k_1^{1310} = (1.1 \pm 0.4) \times 10^{-2} \text{ mW}^{-2} \times P^2$, and $k_{-1}^{1310} = (4.3 \pm 1.6) \times$
302 $10^{-2} \text{ mW}^{-2} \times P^2$ (Fig. 5b). The fitted curves well describe the data, thus lending credence to the underlying
303 model. In particular, the analysis reveals that both the Pr→Pfr photoconversion and the Pfr→Pr reversion
304 can be driven by 2P absorption. The ratio of the rate constants for Pr→Pfr and Pfr→Pr 2P conversion, k_1/k_{-1} ,
305 amounted to 0.55, 0.67 and 0.26, at 1190 nm, 1250 nm and 1310 nm, respectively. Although smaller than
306 the k_1/k_{-1} ratio of $0.69 / 0.31 = 2.2$ obtained for the photoreversible 1P conversion at 680 nm (see Fig. 1c),
307 we consider these values plausible. Notably, the k_1/k_{-1} ratios are directly reflected in the maximally
308 attainable Pfr yields which were lower for 2P conversion (see Fig. 4d) than for 1P conversion (see Fig. 1c).

309 Depending on wavelength, the 2P irradiation exhibited varying maximal Pfr yields. For a quantitative
310 analysis, it is worth noting that the 2P focal volume had a depth of several millimeters and covered the
311 entire path length of the sample cuvette (1 mm). Likewise, the 2P beam waist radius was around 130 μm
312 and thus exceeded the 100 μm radius of the probe beam. Taken together, the absorbance measurements
313 hence record the Pr and Pfr populations inside the 2P focal volume with negligible contribution of the
314 surrounding bulk volume. In the range between 1170 nm and 1280 nm, up to 35-40% Pfr state was
315 obtained inside the focal volume at photostationary state. However, at 1310 nm, the attainable Pfr yield
316 dropped to 25% which could in principle be either due to diminished Pr→Pfr conversion, to elevated
317 Pfr→Pr reversion, or both. As the present data mainly reflect the relative velocities of diffusion and the
318 forward and reverse conversion rather than their absolute values, it is challenging to discriminate between
319 these scenarios. That notwithstanding, our analyses implicate enhanced Pfr→Pr reversion as the principal
320 cause for the reduced Pfr yield at longer 2P wavelengths. These findings overall match those in the 1P
321 regime where longer excitation wavelengths generally lead to smaller Pfr:Pr ratios at photostationary state.
322 However, whereas 1P irradiation with (680 ± 15) nm effectively converted the DdPCM to the Pfr state (see
323 Fig. 1c), 2P irradiation at twice this wavelength did not (with, e.g., a Pfr yield of only 6% at 1370 nm).
324 Intriguingly, the optimum range for photoconversion to the Pfr state in the 2P regime is thus shifted to
325 slightly higher energies than expected based on photoconversion in the 1P regime (see Fig. 4d). Notably,
326 similar spectral shifts towards shorter wavelengths have been reported for the 2P excitation of several
327 fluorescent proteins and have been attributed to non-Condon transitions (57–60). Regardless of the precise
328 origin of the spectral shift, our data reveal that laser wavelengths between 1170 nm and 1300 nm achieve
329 the best Pfr yield, thus informing the actuation of bacterial phytochromes by two-photon absorption.

330 Transcending earlier 2P fluorescence studies (28, 61), we now demonstrate the actuation of bacterial
331 phytochromes by 2P irradiation. Our analyses clearly show that 2P conversion of bacterial phytochromes is
332 feasible in both the Pr→Pfr and Pfr→Pr directions, which paves the way towards novel applications *in vivo*.
333 Notably, an assortment of optogenetic actuators based on bacterial phytochromes are already in place and
334 can be deployed for the regulation of cellular processes including cyclic-nucleotide metabolism, gene
335 expression and subcellular localization (10, 31, 62). Beyond affording superior spatial resolution, the 1.1-1.5
336 μm wavelengths used for 2P activation offer improved penetration through skull and bone (38). For

337 practical application, water absorption, which increases by around tenfold between 1 and 1.5 μm , however
338 needs to be taken into account (63). Taken together, the conversion of bacterial phytochromes by the near-
339 infrared 2P illumination demonstrated here establishes a novel modality for the specific, non-invasive
340 intervention in the brain, complementing alternative approaches based on for instance optogenetics (7–9)
341 and electrogenetics (64).

342

343 Methods

344 Molecular Biology and Protein Expression

345 The gene encoding the *Deinococcus deserti* photosensory core module (*DdPCM*) (WP_012695070.1,
346 residues 1-520) was synthesized with *E. coli*-adapted codon usage (GeneArt, Regensburg, Germany) and
347 cloned into a pCDFDuet plasmid (Novagen, Merck, Darmstadt, Germany) with a C-terminal hexahistidine
348 tag via Gibson assembly (65). The gene encoding *Synechocystis* sp. heme oxygenase 1 (*SsHO*) was amplified
349 by PCR from plasmid pKT270 (66) and cloned by Gibson assembly into the pCDFDuet vector, such that the
350 expression of *DdPCM* and *SsHO* is under control of T7-lacO promoters. The integrity of the construct was
351 confirmed by Sanger DNA sequencing (Microsynth Seqlab, Göttingen, Germany). For expression, the
352 plasmid was transformed into BL21(DE3) cells and used to inoculate two baffled flasks with 800 mL
353 lysogeny broth (LB) medium supplemented with 100 $\mu\text{g mL}^{-1}$ streptomycin (Strep). Bacterial cultures were
354 grown at 37°C and 225 rpm up to an optical density at 600 nm of around 0.6, at which point the
355 temperature was lowered to 16°C and 0.5 mM δ -amino levulinic acid was added. Expression of *DdPCM* and
356 *SsHO* was induced by addition of 1 mM isopropyl β -D-1-thiogalactopyranoside, and cultivation continued at
357 16°C and 225 rpm for 16 h. Purification of *DdPCM* was conducted similar to previous protocols (26, 35). In
358 brief, cells were spun down, resuspended in 50 mM Tris/HCl pH 8.0, 20 mM NaCl, 20 mM imidazole and
359 supplemented with protease inhibitors (cOMplete Ultra, Roche Diagnostics, Mannheim, Germany).
360 Following lysis by microfluidizer and centrifugation, the supernatant was incubated for 1 h at 4°C with 100
361 μM biliverdin hydrochloride (Livchem Logistics GmbH, Frankfurt, Germany) and 5 mM Tris-(2-carboxyethyl)-
362 phosphine. The lysate was then applied to Ni^{2+} -nitrilotriacetic acid affinity resin (Protino Ni-NTA, Macherey
363 & Nagel GmbH, Düren, Germany). After extensive washing of the resin, the bound protein was eluted with
364 200 mM imidazole, pooled and dialyzed into 50 mM Tris/HCl pH 8.0, 20 mM NaCl. Following purification by
365 anion-exchange chromatography (HiTrap Q HP, GE Healthcare, Munich, Germany), the protein purity was
366 analyzed by denaturing polyacrylamide gel electrophoresis (PAGE) and Coomassie staining. Covalent
367 chromophore incorporation was assessed by Zn^{2+} -induced bilin fluorescence (67). Fractions containing pure
368 protein were pooled, dialyzed into storage buffer [50 mM Tris/HCl pH 8.0, 20 mM NaCl, 20% (w/v) glycerol]
369 and concentrated by spin filtration (Vivaspin 6, 10-kDa cutoff, GE Healthcare). Sample concentration was
370 determined by absorbance measurements (8453 UV-vis, Agilent Technologies, Waldbronn, Germany) based
371 on an estimated molar extinction coefficient of 45,700 $\text{M}^{-1} \text{cm}^{-1}$ at the isosbestic point (724 nm) (26). For
372 storage, proteins aliquots were flash-frozen in liquid nitrogen and stored at -80°C.

373 UV-vis absorbance spectra of *DdPCM* were recorded on an Agilent 8435 diode-array spectrophotometer
374 (Agilent Technologies, Waldbronn, Germany) for dark-adapted *DdPCM*, and after irradiation with red [(680
375 \pm 15) nm, 80 $\mu\text{W cm}^{-2}$] of far-red light [(780 \pm 15) nm, 80 $\mu\text{W cm}^{-2}$] for 30 s. The spectrum of the pure Pfr
376 state was calculated according to (68). Pfr \rightarrow Pr recovery kinetics were recorded on a Cary 100 UV-vis
377 spectrophotometer (Agilent Technologies, Waldbronn, Germany) by following absorbance over time at 703,
378 722, and 755 nm after saturating illumination with red light. Data were evaluated and plotted with the Fit-
379 o-mat program (69).

380

381 Computational Methods

382 A homology model of *DdPCM* in the red-absorbing (Pr) dark-adapted state was generated as a starting
383 point for the computational work. The amino acid sequence of *DdPCM* was retrieved from the UniProt
384 Database (Entry: C1D3W9) and compared to related sequences using Swiss-Model (70). The X-ray crystal
385 structure of the BPhy (chain A with a sequence identity of 48%) from *Deinococcus radiodurans* (*DrPCM*) at a
386 resolution of 2.75 Å (PDB code 4Q0J) (52) was selected as the template. The homology model was assessed
387 using MolProbity, which evaluates various aspects such as atomic clashes, sidechain rotamers, and
388 Ramachandran angles and is normalized to be on the same scale as X-ray resolution (71, 72). The obtained
389 score of 1.36 corresponds to 97th percentile and indicates a high-quality model (the 100th percentile is
390 considered the best structure). In addition, the homology model was also inspected visually by overlaying
391 the structure of the BV chromophore binding pocket of the *DrPCM* and the *DdPCM* (Fig. S2). Water
392 molecules from the template structure (4Q0J) were copied into the homology model and relaxed in the
393 MM region during optimization.

394 The homology model was solvated with TIP3P water models in a rectangular box with a distance of at least
395 13.5 Å from any protein atom to the boundary of the box. QM/MM geometry optimization was performed
396 using ChemShell interfaced to the Orca 4.1 program (73). The amino acids and water molecules constitute
397 the MM region and were described using the Amber ff14SB force-field (74). A hydrogen link atom was
398 placed between the C-C atom of the BV chromophore, after the sulfur atom of the covalently linked Cys
399 residue. The QM region was treated at BLYP/cc-pVDZ level of theory with D3BJ dispersion correction in the
400 geometry optimization (75). This method was chosen based on the previous benchmark for the linear
401 tetrapyrrole chromophore such as found in phytochromes (75).

402 The calculation of one-photon absorption (1PA) was done for the 10 lowest excited states. Here, we used
403 the approximate coupled cluster method CC2 with the “resolution of identity” (RI) as implemented in
404 Turbomole 7.3 (76). The basis set aug-cc-pVDZ and the corresponding auxiliary basis set were used, with
405 frozen core orbitals by default. The surrounding environment was treated as point charges.

406 To further assess the reliability of our approach, the 1PA and 2PA calculations were performed on two
407 different sizes of the QM region, as shown in Fig. 2. The smaller QM region (QM65) consists of the BV
408 chromophore with truncated propionate side chains, thus comprising 65 atoms including two additional
409 link atoms to account for the truncation of propionate chains. The larger QM region (biliverdin comprising
410 75 atoms) additionally contains the propionates and is identical to the one used for the geometry
411 optimization. The two-photon absorption (2PA) calculations were performed for the first excited state, at
412 the same level of theory. Estimation of 2PA cross-section was based on equation (4), as illustrated by
413 Beerepoot *et al.* (55).

$$414 \quad \sigma^{TPA} = \frac{N\pi^3\alpha\alpha_0^5\omega^2}{c} \langle \delta^{TPA} \rangle g(2\omega, \omega_0, \Gamma) \quad (4)$$

415 where N is the integer number, α is the fine structure constant, α_0 is the Bohr radius, ω is the photon
416 energy, c is the speed of light, $\langle \delta^{TPA} \rangle$ is the rotationally averaged two-photon transition moment, and $g(2\omega,$
417 $\omega_0, \Gamma)$ is the line shape function. Considering the experimental setup, $N = 4$ and $\Gamma = 0.2$ eV (full-width half
418 maximum) were used in equation (4).

419

420 Quantitative Modelling of Two-photon Photoconversion

421 The transformation of DdPCM by two-photon irradiation was modeled by considering the fractions R and
422 FR of the Pr and Pfr state within the focal volume. During illumination, R and FR change over time t
423 according to:

$$424 \quad dR/dt = -k_1 \times R + k_{-1} \times FR + D \times (R_0 - R) \quad (5)$$

$$425 \quad dFR/dt = k_1 \times R - k_{-1} \times FR + D \times (FR_0 - FR) \quad (6)$$

426 where k_1 and k_{-1} are unimolecular rate constants for the light-driven Pr→Pfr and Pfr→Pr transitions,
427 respectively; the diffusion constant D accounts for diffusion of molecules into and out of the focal volume;
428 and R_0 and FR_0 are the fractions of the Pr and Pfr states in the absence of illumination. Accounting for the
429 two-photon absorption, the velocities of both transitions are assumed to quadratically depend on the
430 photon flux Φ according to:

$$431 \quad k_1 = f_1 \times \Phi^2 \quad (7)$$

$$432 \quad k_{-1} = f_{-1} \times \Phi^2 \quad (8)$$

433 The photon flux is proportional to the applied laser power P according to:

$$434 \quad \Phi = g_\lambda \times P \quad (9)$$

435 where the coefficient g_λ considers the relative energy content and flux density of the photons of the
436 different wavelengths used. Normalized to the value at 1190 nm, the coefficients were $g_{1190} = 1$, $g_{1250} = 0.96$
437 and $g_{1310} = 0.91$.

438 By integration of equations (5) and (6), expression (11) is obtained for the fraction FR inside the laser focal
439 volume at time t :

$$440 \quad FR(t) = R_0 + FR_0 - R_\infty - (R_0 - R_\infty) \times \exp(-\tilde{k} \times t) \quad (10)$$

441 where:

$$442 \quad \tilde{k} = k_1 + D + k_{-1} \quad (11)$$

$$443 \quad R_\infty = k_{-1}/\tilde{k} \times (R_0 + FR_0) + D/\tilde{k} \times R_0 \quad (12)$$

444 At photostationary state, the fraction of FR is hence given by:

$$445 \quad FR_\infty = R_0 + FR_0 - k_{-1}/\tilde{k} \times (R_0 + FR_0) + D/\tilde{k} \times R_0 \quad (13)$$

446 Notably, the steady-state value FR_∞ depends on the ratio of the rate constants D , k_1 and k_{-1} , rather than
447 their individual values. The rate constants were hence taken as dimensionless, and D was fixed at an
448 arbitrary value of 1. The two-photon power dependence data at wavelengths of 1190, 1250 and 1310 nm
449 were globally fitted with Fit-o-mat (69) using individual parameters f_1 and f_{-1} . Fitted parameters were f_1^{1190}
450 $= (1.1 \pm 0.2) \times 10^{-2} \text{ mW}^{-2}$, $f_{-1}^{1190} = (2.0 \pm 0.4) \times 10^{-2} \text{ mW}^{-2}$, $f_1^{1250} = (6.9 \pm 1.0) \times 10^{-3} \text{ mW}^{-2}$, $f_{-1}^{1250} = (1.0 \pm 0.2) \times$
451 10^{-2} mW^{-2} , $f_1^{1310} = (1.4 \pm 0.4) \times 10^{-2} \text{ mW}^{-2}$, and $f_{-1}^{1310} = (5.3 \pm 2.0) \times 10^{-2} \text{ mW}^{-2}$.

452

453 Acknowledgements

454 This project has received funding from the European Union’s H2020 FET OPEN NEUROPA project under the
455 Grant Agreement No. 863214 (E.U.R., S.G.S. and A.M). A.M. gratefully acknowledges funding by the
456 Deutsche Forschungsgemeinschaft (grants MO2192/4-1 and MO2192/7-1). I.S. acknowledges funding by
457 the European Research Council (ERC) under the European Union’s Horizon 2020 research and innovation
458 program (Grant No. 678169 “PhotoMutant”). I.S. thanks the SFB 1078 “Protonation Dynamics in Protein
459 Function” for the Mercator fellowship. R.K.K. acknowledges support from the Lady Davis Trust for the
460 Shunbrun postdoctoral fellowship. N.B.C. has received funding from the EU H2020 research and innovation
461 program under the Marie Skłodowska-Curie (grant agreement No 843801); E.A.Z. acknowledges funding by
462 the Academy of Finland (grant 318281), RFBR (grant 20-08-01153\20), Russian Science Foundation (grant
463 20-75-00123) and the grant of the Russian Federation Government no. 075-15-2019-1877.

464

465 Authors’ contributions

466 E.U.R., S.G.S. and A.M. conceived the project; E.U.R., S.G.S., I.S. and A.M. supervised the work; D.G. and R.S.
467 cloned, expressed, purified and spectroscopically characterized phytochromes; E.A.Z., N.C., and A.G.
468 performed two-photon conversion experiments; R.K.K. constructed the homology model and calculated 1P
469 and 2P absorbance spectra; R.K.K. and I.S. analyzed the quantum chemical calculations; A.M. and E.A.Z.
470 developed the analytical model for 2P excitation; A.M., E.U.R., S.G.S., E.A.Z., I.S., R.K.K. interpreted the
471 results; A.M., S.G.S., E.A.Z., E.U.R., R.K.K. and I.S. wrote the manuscript with input from all authors.

472

473 Competing interests

474 The authors declare no conflict of interests.

475

476 References

- 477 1. Hegemann, P. 2008. Algal sensory photoreceptors. *Annu. Rev. Plant Biol.* 59:167–189.
- 478 2. Möglich, A., X. Yang, R.A. Ayers, and K. Moffat. 2010. Structure and function of plant
479 photoreceptors. *Annu. Rev. Plant Biol.* 61:21–47.
- 480 3. Deisseroth, K., G. Feng, A.K. Majewska, G. Miesenböck, A. Ting, and M.J. Schnitzer. 2006.
481 Next-generation optical technologies for illuminating genetically targeted brain circuits. *J.*
482 *Neurosci.* 26:10380–10386.
- 483 4. Nagel, G., D. Ollig, M. Fuhrmann, S. Kateriya, A.M. Musti, E. Bamberg, and P. Hegemann.
484 2002. Channelrhodopsin-1: a light-gated proton channel in green algae. *Science.* 296:2395–
485 2398.
- 486 5. Nagel, G., T. Szellas, W. Huhn, S. Kateriya, N. Adeishvili, P. Berthold, D. Ollig, P. Hegemann,
487 and E. Bamberg. 2003. Channelrhodopsin-2, a directly light-gated cation-selective membrane
488 channel. *Proc. Natl. Acad. Sci. U. S. A.* 100:13940–13945.
- 489 6. Losi, A., K.H. Gardner, and A. Möglich. 2018. Blue-Light Receptors for Optogenetics. *Chem.*
490 *Rev.* 118:10659–10709.

-
- 491 7. Klapoetke, N.C., Y. Murata, S.S. Kim, S.R. Pulver, A. Birdsey-Benson, Y.K. Cho, T.K. Morimoto,
492 A.S. Chuong, E.J. Carpenter, Z. Tian, J. Wang, Y. Xie, Z. Yan, Y. Zhang, B.Y. Chow, B. Surek, M.
493 Melkonian, V. Jayaraman, M. Constantine-Paton, G.K.-S. Wong, and E.S. Boyden. 2014.
494 Independent optical excitation of distinct neural populations. *Nat. Methods*. 11:338–346.
- 495 8. Oda, K., J. Vierock, S. Oishi, S. Rodriguez-Rozada, R. Taniguchi, K. Yamashita, J.S. Wiegert, T.
496 Nishizawa, P. Hegemann, and O. Nureki. 2018. Crystal structure of the red light-activated
497 channelrhodopsin Chrimson. *Nat. Commun*. 9:3949.
- 498 9. Gong, X., D. Mendoza-Halliday, J.T. Ting, T. Kaiser, X. Sun, A.M. Bastos, R.D. Wimmer, B. Guo,
499 Q. Chen, Y. Zhou, M. Pruner, C.W.-H. Wu, D. Park, K. Deisseroth, B. Barak, E.S. Boyden, E.K.
500 Miller, M.M. Halassa, Z. Fu, G. Bi, R. Desimone, and G. Feng. 2020. An Ultra-Sensitive Step-
501 Function Opsin for Minimally Invasive Optogenetic Stimulation in Mice and Macaques.
502 *Neuron*. 107:38-51.e8.
- 503 10. Gourinchas, G., S. Ettl, and A. Winkler. 2019. Bacteriophytochromes – from informative
504 model systems of phytochrome function to powerful tools in cell biology. *Curr. Opin. Struct.*
505 *Biol*. 57:72–83.
- 506 11. Weissleder, R. 2001. A clearer vision for *in vivo* imaging. *Nat. Biotechnol*. 19:316–317.
- 507 12. Butler, W.L., K.H. Norris, H.W. Siegelman, and S.B. Hendricks. 1959. Detection, Assay, and
508 Preliminary Purification of the Pigment Controlling Photoresponsive Development of Plants.
509 *Proc. Natl. Acad. Sci*. 45:1703–1708.
- 510 13. Rockwell, N.C., and J.C. Lagarias. 2010. A brief history of phytochromes. *Chemphyschem*.
511 11:1172–1180.
- 512 14. Rockwell, N.C., and J.C. Lagarias. 2020. Phytochrome evolution in 3D: deletion, duplication,
513 and diversification. *New Phytol*. 225:2283–2300.
- 514 15. Möglich, A., R.A. Ayers, and K. Moffat. 2009. Structure and signaling mechanism of Per-ARNT-
515 Sim domains. *Structure*. 17:1282–1294.
- 516 16. Aravind, L., and C.P. Ponting. 1997. The GAF domain: an evolutionary link between diverse
517 phototransducing proteins. *Trends Biochem Sci*. 22:458–9.
- 518 17. Yang, X., J. Kuk, and K. Moffat. 2008. Crystal structure of *Pseudomonas aeruginosa*
519 bacteriophytochrome: Photoconversion and signal transduction. *Proc Natl Acad Sci U A*.
520 105:14715–14720.
- 521 18. Essen, L.O., J. Mailliet, and J. Hughes. 2008. The structure of a complete phytochrome
522 sensory module in the Pr ground state. *Proc Natl Acad Sci U A*. 105:14709–14714.
- 523 19. Takala, H., A. Björling, O. Berntsson, H. Lehtivuori, S. Niebling, M. Hoernke, I. Kosheleva, R.
524 Henning, A. Menzel, J.A. Ihalainen, and S. Westenhoff. 2014. Signal amplification and
525 transduction in phytochrome photosensors. *Nature*. 509:245–248.
- 526 20. Burgie, E.S., J. Zhang, and R.D. Vierstra. 2016. Crystal Structure of *Deinococcus* Phytochrome
527 in the Photoactivated State Reveals a Cascade of Structural Rearrangements during
528 Photoconversion. *Structure*. 24:448–457.
- 529 21. Möglich, A. 2019. Signal transduction in photoreceptor histidine kinases. *Protein Sci*.
530 28:1923–1946.
- 531 22. Ni, M., J.M. Tepperman, and P.H. Quail. 1998. PIF3, a phytochrome-interacting factor
532 necessary for normal photoinduced signal transduction, is a novel basic helix-loop-helix
533 protein. *Cell*. 95:657–667.
-

-
- 534 23. Pham, V.N., P.K. Kathare, and E. Huq. 2018. Phytochromes and Phytochrome Interacting
535 Factors. *Plant Physiol.* 176:1025–1038.
- 536 24. Golonka, D., P. Fischbach, S.G. Jena, J.R.W. Kleeberg, L.-O. Essen, J.E. Toettcher, M.D.
537 Zurbriggen, and A. Möglich. 2019. Deconstructing and repurposing the light-regulated
538 interplay between Arabidopsis phytochromes and interacting factors. *Commun. Biol.* 2:448.
- 539 25. Golonka, D., U. Gerken, J. Köhler, and A. Möglich. 2020. The Association Kinetics Encode the
540 Light Dependence of Arabidopsis Phytochrome B Interactions. *J. Mol. Biol.* 432:4327–4340.
- 541 26. Gasser, C., S. Taiber, C.-M. Yeh, C.H. Wittig, P. Hegemann, S. Ryu, F. Wunder, and A. Möglich.
542 2014. Engineering of a red-light-activated human cAMP/cGMP-specific phosphodiesterase.
543 *Proc. Natl. Acad. Sci. U. S. A.* 111:8803–8808.
- 544 27. Stüven, B., R. Stabel, R. Ohlendorf, J. Beck, R. Schubert, and A. Möglich. 2019.
545 Characterization and engineering of photoactivated adenylyl cyclases. *Biol. Chem.* 400:429–
546 441.
- 547 28. Piatkevich, K.D., F.V. Subach, and V.V. Verkhusha. 2013. Engineering of bacterial
548 phytochromes for near-infrared imaging, sensing, and light-control in mammals. *Chem. Soc.*
549 *Rev.* 42:3441–3452.
- 550 29. Ryu, M.-H., I.-H. Kang, M.D. Nelson, T.M. Jensen, A.I. Lyuksyutova, J. Siltberg-Liberles, D.M.
551 Raizen, and M. Gomelsky. 2014. Engineering adenylyl cyclases regulated by near-infrared
552 window light. *Proc. Natl. Acad. Sci. U. S. A.* 111:10167–10172.
- 553 30. Etzl, S., R. Lindner, M.D. Nelson, and A. Winkler. 2018. Structure-guided design and functional
554 characterization of an artificial red light–regulated guanylate/adenylyl cyclase for
555 optogenetic applications. *J. Biol. Chem.* 293:9078–9089.
- 556 31. Shcherbakova, D.M., A.A. Shemetov, A.A. Kaberniuk, and V.V. Verkhusha. 2015. Natural
557 Photoreceptors as a Source of Fluorescent Proteins, Biosensors, and Optogenetic Tools.
558 *Annu. Rev. Biochem.* 84:519–550.
- 559 32. Ziegler, T., and A. Möglich. 2015. Photoreceptor engineering. *Front. Mol. Biosci.* 2:30.
- 560 33. Filonov, G.S., K.D. Piatkevich, L.-M. Ting, J. Zhang, K. Kim, and V.V. Verkhusha. 2011. Bright
561 and stable near-infrared fluorescent protein for in vivo imaging. *Nat. Biotechnol.* 29:757–761.
- 562 34. Ryu, M.-H., and M. Gomelsky. 2014. Near-infrared light responsive synthetic c-di-GMP
563 module for optogenetic applications. *ACS Synth. Biol.* 3:802–810.
- 564 35. Stabel, R., B. Stüven, J.N. Hansen, H.G. Körschen, D. Wachten, and A. Möglich. 2019.
565 Revisiting and Redesigning Light-Activated Cyclic-Mononucleotide Phosphodiesterases. *J.*
566 *Mol. Biol.* 431:3029–3045.
- 567 36. Kaberniuk, A.A., A.A. Shemetov, and V.V. Verkhusha. 2016. A bacterial phytochrome-based
568 optogenetic system controllable with near-infrared light. *Nat. Methods.* 13:591–597.
- 569 37. Redchuk, T.A., A.A. Kaberniuk, and V.V. Verkhusha. 2018. Near-infrared light–controlled
570 systems for gene transcription regulation, protein targeting and spectral multiplexing. *Nat.*
571 *Protoc.* 13:1121–1136.
- 572 38. Golovynskyi, S., I. Golovynska, L.I. Stepanova, O.I. Datsenko, L. Liu, J. Qu, and T.Y.
573 Ohulchanskyy. 2018. Optical windows for head tissues in near-infrared and short-wave
574 infrared regions: Approaching transcranial light applications. *J. Biophotonics.* 11:e201800141.
- 575 39. Bashkatov, A.N., E.A. Genina, V.I. Kochubey, and V.V. Tuchin. 2006. Optical properties of
576 human cranial bone in the spectral range from 800 to 2000 nm. In: Saratov Fall Meeting
-

-
- 577 2005: Optical Technologies in Biophysics and Medicine VII. International Society for Optics
578 and Photonics. p. 616310.
- 579 40. Hong, G., S. Diao, J. Chang, A.L. Antaris, C. Chen, B. Zhang, S. Zhao, D.N. Atochin, P.L. Huang,
580 K.I. Andreasson, C.J. Kuo, and H. Dai. 2014. Through-skull fluorescence imaging of the brain in
581 a new near-infrared window. *Nat. Photonics*. 8:723–730.
- 582 41. Piatkevich, K.D., H.-J. Suk, S.B. Kodandaramaiah, F. Yoshida, E.M. DeGennaro, M. Drobizhev,
583 T.E. Hughes, R. Desimone, E.S. Boyden, and V.V. Verkhusha. 2017. Near-Infrared Fluorescent
584 Proteins Engineered from Bacterial Phytochromes in Neuroimaging. *Biophys. J.* 113:2299–
585 2309.
- 586 42. Forli, A., D. Vecchia, N. Binini, F. Succol, S. Bovetti, C. Moretti, F. Nespoli, M. Mahn, C.A.
587 Baker, M.M. Bolton, O. Yizhar, and T. Fellin. 2018. Two-Photon Bidirectional Control and
588 Imaging of Neuronal Excitability with High Spatial Resolution In Vivo. *Cell Rep.* 22:3087–3098.
- 589 43. dal Maschio, M., J.C. Donovan, T.O. Helmbrecht, and H. Baier. 2017. Linking Neurons to
590 Network Function and Behavior by Two-Photon Holographic Optogenetics and Volumetric
591 Imaging. *Neuron*. 94:774-789.e5.
- 592 44. Yang, W., L. Carrillo-Reid, Y. Bando, D.S. Peterka, and R. Yuste. 2018. Simultaneous two-
593 photon imaging and two-photon optogenetics of cortical circuits in three dimensions. *eLife*.
594 7:e32671.
- 595 45. Prakash, R., O. Yizhar, B. Grewe, C. Ramakrishnan, N. Wang, I. Goshen, A.M. Packer, D.S.
596 Peterka, R. Yuste, M.J. Schnitzer, and K. Deisseroth. 2012. Two-photon optogenetic toolbox
597 for fast inhibition, excitation and bistable modulation. *Nat. Methods*. 9:1171–1179.
- 598 46. Yeh, K.-C., S.-H. Wu, J.T. Murphy, and J.C. Lagarias. 1997. A Cyanobacterial Phytochrome Two-
599 Component Light Sensory System. *Science*. 277:1505–1508.
- 600 47. Hughes, J., T. Lamparter, F. Mittmann, E. Hartmann, W. Gärtner, A. Wilde, and T. Börner.
601 1997. A prokaryotic phytochrome. *Nature*. 386:663.
- 602 48. Davis, S.J., A.V. Vener, and R.D. Vierstra. 1999. Bacteriophytochromes: Phytochrome-Like
603 Photoreceptors from Nonphotosynthetic Eubacteria. *Science*. 286:2517–2520.
- 604 49. Bhoo, S.-H., S.J. Davis, J. Walker, B. Karniol, and R.D. Vierstra. 2001. Bacteriophytochromes
605 are photochromic histidine kinases using a biliverdin chromophore. *Nature*. 414:776–779.
- 606 50. Wagner, J.R., J.S. Brunzelle, K.T. Forest, and R.D. Vierstra. 2005. A light-sensing knot revealed
607 by the structure of the chromophore-binding domain of phytochrome. *Nature*. 438:325–331.
- 608 51. Multamäki, E., R. Nanekar, D. Morozov, T. Lievonen, D. Golonka, W.Y. Wahlgren, B. Stucki-
609 Buchli, J. Rossi, V.P. Hytönen, S. Westenhoff, J.A. Ihalainen, A. Möglich, and H. Takala. 2020.
610 Illuminating a Phytochrome Paradigm – a Light-Activated Phosphatase in Two-Component
611 Signaling Uncovered. *bioRxiv*. 2020.06.26.173310.
- 612 52. Burgie, E.S., T. Wang, A.N. Bussell, J.M. Walker, H. Li, and R.D. Vierstra. 2014. Crystallographic
613 and Electron Microscopic Analyses of a Bacterial Phytochrome Reveal Local and Global
614 Rearrangements during Photoconversion. *J. Biol. Chem.* 289:24573–24587.
- 615 53. Wiebeler, C., A.G. Rao, W. Gärtner, and I. Schapiro. 2019. The Effective Conjugation Length Is
616 Responsible for the Red/Green Spectral Tuning in the Cyanobacteriochrome Slr1393g3.
617 *Angew. Chem. Int. Ed.* 58:1934–1938.
- 618 54. Church, J.R., A.G. Rao, A. Barnoy, C. Wiebeler, and I. Schapiro. Computational Studies of
619 Photochemistry in Phytochrome Proteins. In: QM/MM Studies of Light-responsive Biological
620 Systems. .
-

-
- 621 55. Beerepoot, M.T.P., D.H. Frieze, N.H. List, J. Kongsted, and K. Ruud. 2015. Benchmarking two-
622 photon absorption cross sections: performance of CC2 and CAM-B3LYP. *Phys. Chem. Chem.*
623 *Phys.* 17:19306–19314.
- 624 56. Grabarek, D., and T. Andruniów. 2019. Assessment of Functionals for TDDFT Calculations of
625 One- and Two-Photon Absorption Properties of Neutral and Anionic Fluorescent Proteins
626 Chromophores. *J. Chem. Theory Comput.* 15:490–508.
- 627 57. Hosoi, H., S. Yamaguchi, H. Mizuno, A. Miyawaki, and T. Tahara. 2008. Hidden Electronic
628 Excited State of Enhanced Green Fluorescent Protein. *J. Phys. Chem. B.* 112:2761–2763.
- 629 58. Drobizhev, M., S. Tillo, N.S. Makarov, T.E. Hughes, and A. Rebane. 2009. Absolute Two-
630 Photon Absorption Spectra and Two-Photon Brightness of Orange and Red Fluorescent
631 Proteins. *J. Phys. Chem. B.* 113:855–859.
- 632 59. Kamarchik, E., and A.I. Krylov. 2011. Non-Condon Effects in the One- and Two-Photon
633 Absorption Spectra of the Green Fluorescent Protein. *J. Phys. Chem. Lett.* 2:488–492.
- 634 60. Homans, R.J., R.U. Khan, M.B. Andrews, A.E. Kjeldsen, L.S. Natrajan, S. Marsden, E.A.
635 McKenzie, J.M. Christie, and A.R. Jones. 2018. Two photon spectroscopy and microscopy of
636 the fluorescent flavoprotein, iLOV. *Phys. Chem. Chem. Phys.* 20:16949–16955.
- 637 61. Piatkevich, K.D., F.V. Subach, and V.V. Verkhusha. 2013. Far-red light photoactivatable near-
638 infrared fluorescent proteins engineered from a bacterial phytochrome. *Nat. Commun.*
639 4:2153.
- 640 62. Shcherbakova, D.M., O.V. Stepanenko, K.K. Turoverov, and V.V. Verkhusha. 2018. Near-
641 Infrared Fluorescent Proteins: Multiplexing and Optogenetics across Scales. *Trends*
642 *Biotechnol.* 36:1230–1243.
- 643 63. Hale, G.M., and M.R. Querry. 1973. Optical Constants of Water in the 200-nm to 200- μ m
644 Wavelength Region. *Appl. Opt.* 12:555–563.
- 645 64. Krawczyk, K., S. Xue, P. Buchmann, G. Charpin-El-Hamri, P. Saxena, M.-D. Husherr, J. Shao, H.
646 Ye, M. Xie, and M. Fussenegger. 2020. Electrogenetic cellular insulin release for real-time
647 glycemic control in type 1 diabetic mice. *Science.* 368:993–1001.
- 648 65. Gibson, D.G., L. Young, R.-Y. Chuang, J.C. Venter, C.A. Hutchison, and H.O. Smith. 2009.
649 Enzymatic assembly of DNA molecules up to several hundred kilobases. *Nat. Methods.* 6:343–
650 345.
- 651 66. Mukougawa, K., H. Kanamoto, T. Kobayashi, A. Yokota, and T. Kohchi. 2006. Metabolic
652 engineering to produce phytochromes with phytochromobilin, phycocyanobilin, or
653 phycoerythrobilin chromophore in *Escherichia coli*. *FEBS Lett.* 580:1333–1338.
- 654 67. Berkelman, T.R., and J.C. Lagarias. 1986. Visualization of bilin-linked peptides and proteins in
655 polyacrylamide gels. *Anal. Biochem.* 156:194–201.
- 656 68. Butler, W.L., S.B. Hendricks, and H.W. Siegelman. 1964. ACTTON SPECTRA OF PHYTOCHROME
657 IN VITRO. *Photochem. Photobiol.* 3:521–528.
- 658 69. Möglich, A. 2018. An Open-Source, Cross-Platform Resource for Nonlinear Least-Squares
659 Curve Fitting. *J. Chem. Educ.* 95:2273–2278.
- 660 70. Waterhouse, A., M. Bertoni, S. Bienert, G. Studer, G. Tauriello, R. Gumienny, F.T. Heer, T.A.P.
661 de Beer, C. Rempfer, L. Bordoli, R. Lepore, and T. Schwede. 2018. SWISS-MODEL: homology
662 modelling of protein structures and complexes. *Nucleic Acids Res.* 46:W296–W303.
-

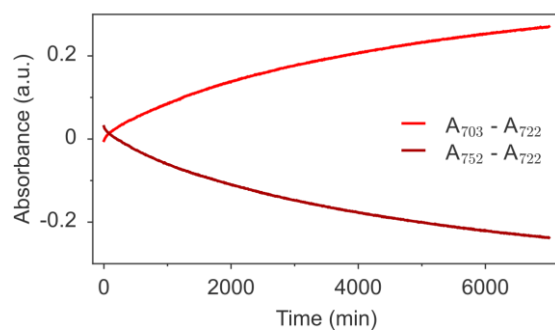
-
- 663 71. Hintze, B.J., S.M. Lewis, J.S. Richardson, and D.C. Richardson. 2016. Molprobity's ultimate
664 rotamer-library distributions for model validation. *Proteins Struct. Funct. Bioinforma.*
665 84:1177–1189.
- 666 72. Williams, C.J., J.J. Headd, N.W. Moriarty, M.G. Prisant, L.L. Videau, L.N. Deis, V. Verma, D.A.
667 Keedy, B.J. Hintze, V.B. Chen, S. Jain, S.M. Lewis, W.B. Arendall, J. Snoeyink, P.D. Adams, S.C.
668 Lovell, J.S. Richardson, and D.C. Richardson. 2018. MolProbity: More and better reference
669 data for improved all-atom structure validation. *Protein Sci.* 27:293–315.
- 670 73. Lu, Y., M.R. Farrow, P. Fayon, A.J. Logsdail, A.A. Sokol, C.R.A. Catlow, P. Sherwood, and T.W.
671 Keal. 2019. Open-Source, Python-Based Redevelopment of the ChemShell Multiscale
672 QM/MM Environment. *J. Chem. Theory Comput.* 15:1317–1328.
- 673 74. Maier, J.A., C. Martinez, K. Kasavajhala, L. Wickstrom, K.E. Hauser, and C. Simmerling. 2015.
674 ff14SB: Improving the Accuracy of Protein Side Chain and Backbone Parameters from ff99SB.
675 *J. Chem. Theory Comput.* 11:3696–3713.
- 676 75. Wiebeler, C., and I. Schapiro. 2019. QM/MM Benchmarking of Cyanobacteriochrome
677 Slr1393g3 Absorption Spectra. *Molecules.* 24:1720.
- 678 76. Balasubramani, S.G., G.P. Chen, S. Coriani, M. Diedenhofen, M.S. Frank, Y.J. Franzke, F.
679 Furche, R. Grotjahn, M.E. Harding, C. Hättig, A. Hellweg, B. Helmich-Paris, C. Holzer, U.
680 Huniar, M. Kaupp, A. Marefat Khah, S. Karbalaei Khani, T. Müller, F. Mack, B.D. Nguyen, S.M.
681 Parker, E. Perlt, D. Rappoport, K. Reiter, S. Roy, M. Rückert, G. Schmitz, M. Sierka, E.
682 Tapavicza, D.P. Tew, C. van Wüllen, V.K. Voora, F. Weigend, A. Wodyński, and J.M. Yu. 2020.
683 TURBOMOLE: Modular program suite for ab initio quantum-chemical and condensed-matter
684 simulations. *J. Chem. Phys.* 152:184107.
- 685

686 **Supplementary Information**

687 **Supplementary Computational Results**

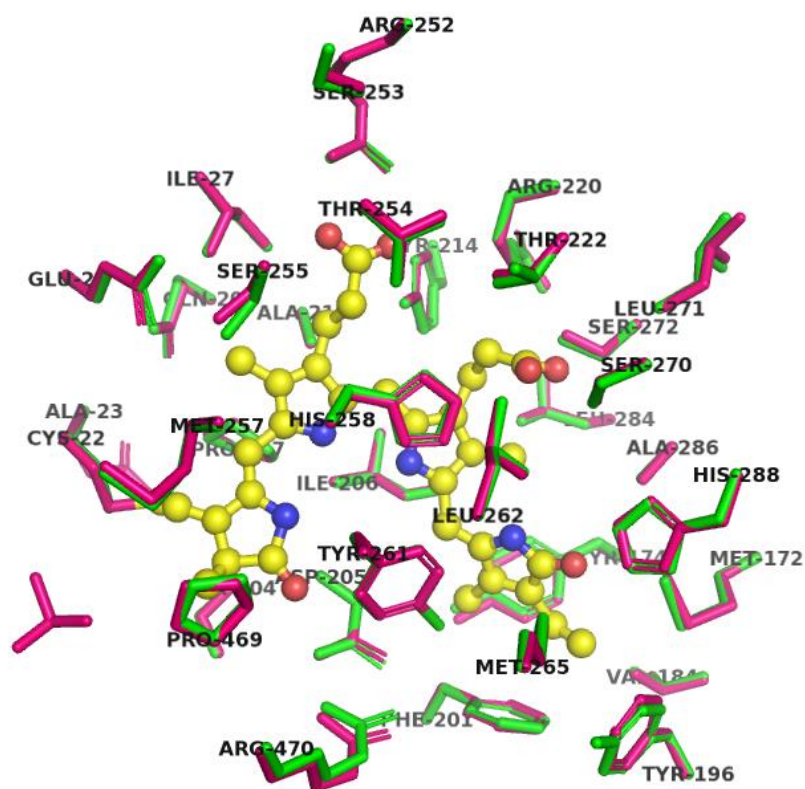
688 A reduced QM region (QM65) was also considered in our calculation to understand the role of the
689 propionate sidechains of biliverdin in the vertical excitation energies. The Q band in QM65 constitutes the
690 transition to the S_1 state whereas the Soret band corresponds to that to the S_5 state. We deduce from the
691 comparison between the QM65 and full biliverdin simulations that only one dark state is due to the
692 presence of the propionate group (Tables S1 and S2).

693 In the 2PA calculation for QM65, at 5258 a.u. the δ^{TPA} was slightly lower than the value for the full
694 chromophore. The σ^{TPA} obtained from the simulation is 7.184 GM. However, the 2PA energy was found to
695 be 0.97 eV which is similar to that of the full chromophore, indicating that truncation of the propionate side
696 chains has no effect on the vertical excitation energies (Figure S4).



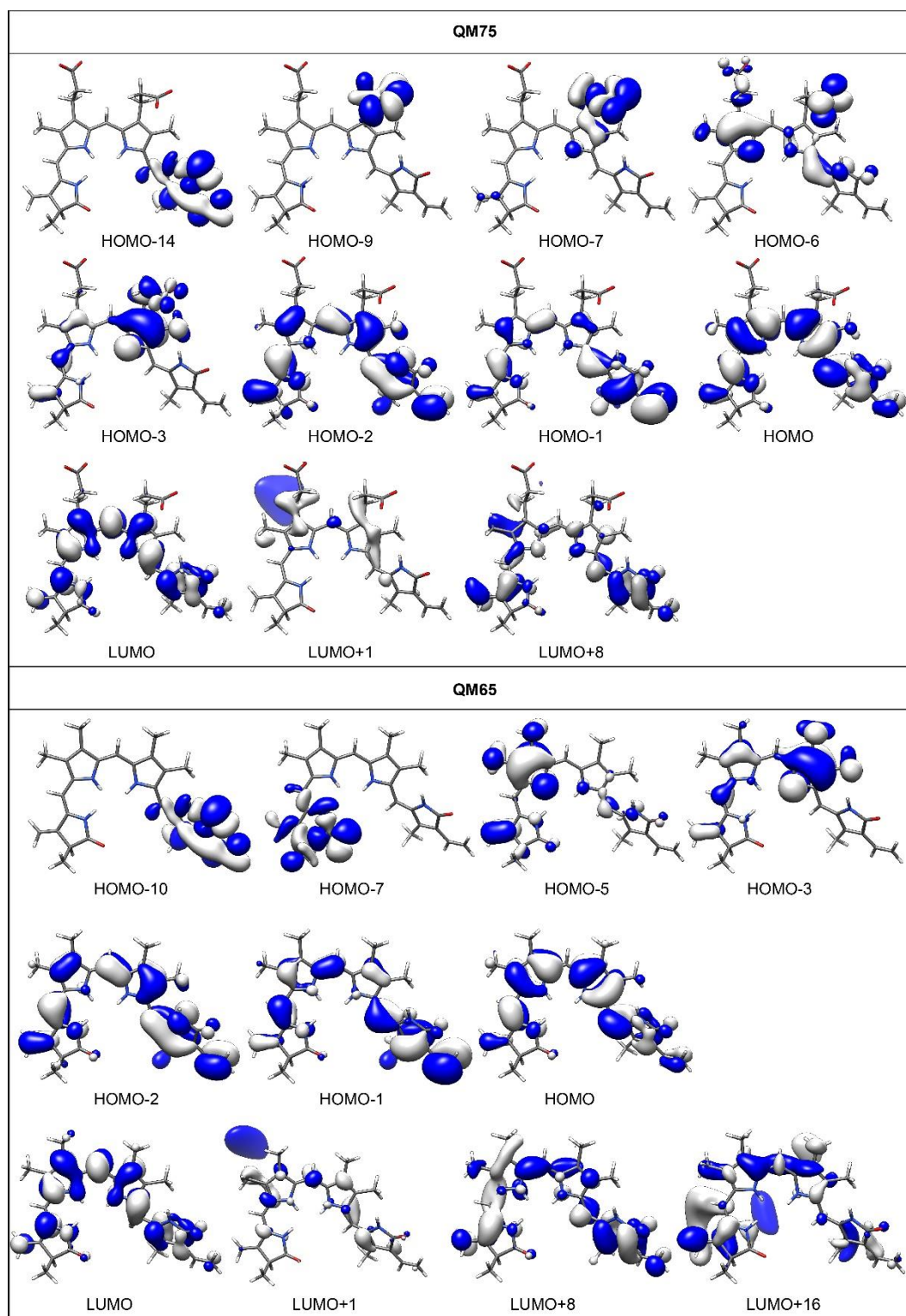
697

698 **Figure S1** | Recovery kinetics of *DdPCM* at 22°C after illumination with red light [(680 ± 15) nm]. The
699 recovery reaction was followed UV-vis-spectroscopically at the absorbance maxima of the Pr and Pfr states,
700 respectively (703 and 752 nm). Data were corrected for spectral drift by the absorbance at the isosbestic
701 point at 722 nm.



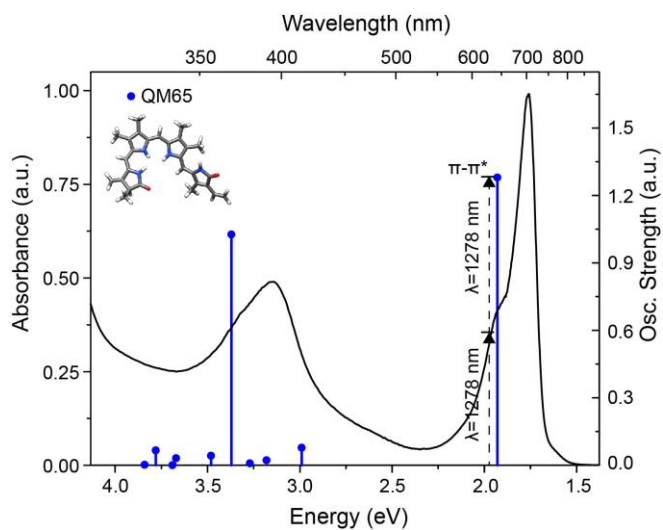
702

703 **Figure S2** | Structural alignment of the biliverdin binding pocket in the *D. deserti* PCM homology model
 704 (green) and the template *D. radiodurans* PCM (PDB 4Q0J) (pink). The amino acids in the 5Å region near the
 705 chromophore are shown with numbering according to the residue position in the sequence of *D. deserti*,
 706 and the BV chromophore is drawn in yellow.



707

708 **Figure S3** | Molecular orbitals involved in the transition of ten low-lying excited states, for biliverdin (upper
 709 panel) and the reduced model QM65 (lower panel).



710

711 **Figure S4** | The experimentally measured Pr absorbance spectrum of *DdPCM* (black line) and the vertical
 712 excitation energies calculated for the reduced QM65 model (stick representation). The height of the sticks
 713 is determined by the oscillator strength. The two-photon excitation energy is marked as a dashed stick. The
 714 optimized geometry of the reduced chromophore (QM65) is shown in the inset.

Biliverdin					
States	Energy (eV)	Wavelength (nm)	Oscillator Strength (<i>f</i>)	Transition type	Molecular Orbitals
S1	1.94	639	1.374	$\pi \rightarrow \pi^*$	HOMO \rightarrow LUMO
S2	2.97	417	0.097	$\pi \rightarrow \pi^*$	HOMO-1 \rightarrow LUMO
S3	3.05	407	0.011	$\pi \rightarrow \pi^*$	HOMO-3 \rightarrow LUMO
S4	3.14	395	0.023	$\pi \rightarrow \pi^*$	HOMO-2 \rightarrow LUMO
S5	3.24	383	0.006	$n \rightarrow \pi^*$	HOMO-9 \rightarrow LUMO
S6	3.38	367	1.074	$\pi \rightarrow \pi^*$	HOMO \rightarrow LUMO+8
S7	3.45	359	0.016	$n \rightarrow \pi^*$	HOMO-7 \rightarrow LUMO
S8	3.57	347	0.003	$\pi \rightarrow \pi^*$	HOMO \rightarrow LUMO+1
S9	3.64	341	0.056	$n \rightarrow \pi^*$	HOMO-14 \rightarrow LUMO
S10	3.66	339	0.003	$\pi \rightarrow \pi^*$	HOMO-6 \rightarrow LUMO
QM65					
States	Energy (eV)	Wavelength (nm)	Oscillator Strength (<i>f</i>)	Transition type	Molecular Orbitals
S1	1.93	642	1.281	$\pi \rightarrow \pi^*$	HOMO \rightarrow LUMO
S2	2.99	415	0.079	$\pi \rightarrow \pi^*$	HOMO-1 \rightarrow LUMO
S3	3.18	390	0.023	$\pi \rightarrow \pi^*$	HOMO-2 \rightarrow LUMO
S4	3.27	379	0.009	$\pi \rightarrow \pi^*$	HOMO-3 \rightarrow LUMO
S5	3.37	368	1.027	$\pi \rightarrow \pi^*$	HOMO \rightarrow LUMO+8
S6	3.48	356	0.043	$\pi \rightarrow \pi^*$	HOMO \rightarrow LUMO+1
S7	3.67	338	0.032	$n \rightarrow \pi^*$	HOMO-10 \rightarrow LUMO
S8	3.69	336	0.001	$\pi \rightarrow \pi^*$	HOMO-5 \rightarrow LUMO
S9	3.78	328	0.067	$\pi \rightarrow \pi^*$	HOMO \rightarrow LUMO+16
S10	3.84	323	0.003	$n \rightarrow \pi^*$	HOMO-7 \rightarrow LUMO

717 **Table S2** | Calculated 1PA and 2PA excitation energies for the Q and Soret bands. The calculations were
718 performed at the RI-CC2/aug-cc-pVDZ level of theory. QM65 denotes a biliverdin chromophore with the
719 propionate sidechains omitted from the QM region.

QM65	1PA		2PA		
	Energy (eV)	Oscillator Strength (<i>f</i>)	Energy (eV)	δ^{TPA} (a.u.)	σ^{TPA} (GM)
Q band	1.93	1.281	0.97	5258	7.184
Soret band	3.37	1.027			

720